Fjord circulation induced by melting icebergs

Kenneth G. Hughes[1]

[1]College of Earth, Ocean, and Atmospheric Sciences, Oregon State University, Oregon, USA

Correspondence: Kenneth Hughes (kenneth.hughes@oregonstate.edu)

Abstract.

In an iceberg-choked fjord, meltwater can drive circulation. Down-fjord of the ice, buoyancy and rotation lead to an outflowing surface coastal current hugging one side of the fjord with an inflowing counter current below. To predict the structure and evolution of these currents, we develop an analytical model—complemented by numerical simulations—that involves a rectangular fjord initially at rest. Specifically, we (i) start with the so-called Rossby adjustment problem, (ii) reconfigure it for a closed channel with stratification, and (iii) generalize the conventional 'dam-break' scenario to a gradual-release one that mimics the continual, slow injection of meltwater. Implicit in this description is the result that circulation is mediated by internal Kelvin waves. The analytical model shows that if the total meltwater flux increases (e.g., a larger mélange, warmer water, or enhanced ice–ocean turbulence), then circulation strength increases as would be expected. For realistic parameters, a given meltwater flux induces an exchange flow that is $\sim$50 times larger. This factor decreases with increasing water column stratification and vice versa. Overall, this paper is a step toward making Greenland-wide predictions of fjord inflows and outflows induced by icebergs.

1 Introduction

'Nowhere in the sea could a melting iceberg be expected to have a more pronounced effect on its environment than in the enclosure of a fjord' (Gade, 1979). In Greenland, many fjords house hundreds or thousands of icebergs. For example, Sermilik Fjord—a 100 km long fjord in southeast Greenland—is home to $\mathcal{O}(10\,000)$ icebergs at any given time. Their cumulative freshwater flux of $\sim$500 m^3 s^{-1} is equivalent to a moderately large river (Moon et al., 2018; Moyer et al., 2019; Rezvanbehbahani et al., 2020).

The obvious consequences of iceberg melt are cooling and freshening of near-surface waters. Less obvious are the consequences for circulation. As Enderlin et al. (2016) noted, fjord circulation studies 'have largely ignored the contribution of iceberg melt'. Similarly, Beaird et al. (2017) noted a lack of work on the impact of 'distributed buoyancy forcing on fjord circulation' in Ilulissat Icefjord.

By comparison, there is an abundance of information on how glacial fjords respond to their other dominant source of freshwater, namely subglacial discharge. We know the influence of discharge strength (Cowton et al., 2015; Slater et al., 2016), discharge geometry (Kimura et al., 2014; Carroll et al., 2015; Slater et al., 2015; Jackson et al., 2017), water column stratification (De Andrés et al., 2020), ocean thermal forcing (Xu et al., 2012, 2013), numerical model grid resolution (Sciascia et al., 2013), fjord geometry (Carroll et al., 2017), and the difference between subglacial discharge and river runoff (Bendtsen et al., 2015). With this much accumulated understanding, one can make credible, continent-wide predictions of the total outflow induced by subglacial discharge (Slater et al., 2022).

Perhaps the same level of understanding is possible for iceberg-melt-induced flows. Davison et al. (2020) were the first to address the issue by developing a model of Sermilik Fjord that parameterized iceberg thermodynamics at the sub-grid scale. They predicted that the outflow velocity over the top $\sim$200 m is a few cm s^{-1}, and that the compensating inflow over the 200–500 m depth range increases advection of warm Atlantic Water toward the glaciers at the head of the fjord. Subsequent studies have used the same parameterization in other realistic and idealized settings (Davison et al., 2022; Kajanto et al., 2023; Hager et al., 2023).

It is easy to intuit the idea that meltwater is buoyant and therefore rises up and out of the fjord at the surface and that a compensating inflow is needed at depth. But this does not help with more quantitative questions. Why are the currents the speeds they are? What controls the depths of the inflow and outflow? What would happen in wider or narrower channels? How would results change with different stratification or a different melt parameterization? These questions have yet to be addressed in detail.

The core contribution of this paper is an analytical model explaining the first-order dynamics of a fjord's response to hundreds of melting icebergs. To gain process-level insight and make the problem tractable, we use a semi-realistic approach. For example, the fjord has a realistic width and depth but is idealized as a rectangle. And the icebergs have realistic sizes, but are distributed such that there is a clear line separating mélange and open water. Further, we ignore other forcings like subglacial discharge and

shelf-driven baroclinic flow, and we investigate the initial value problem of a fjord starting from rest. These
simplifications let us best illustrate the role of waves in setting the circulation.

Before presenting the analytical model, we develop and run a high-resolution numerical model of the
same semi-realistic scenario (Section 2). This provides a specific realization, or *answer*, that we then
reverse-engineer. After developing the analytical model in ten steps (Section 3), we test its skill against the
numerical model (Section 4), and then use it in a parameter space study (Section 5).

2   The numerical model

2.1   Numerical model setup

We simulate the dynamics of a rectangular fjord that is $600\,\text{m}$ deep (H) and $5\,\text{km}$ wide (half-width
$W = 2.5\,\text{km}$) using the MITgcm (Marshall et al., 1997; Adcroft et al., 2004). The domain extends $200\,\text{km}$
in the along-fjord (east–west) direction, and in the first $8\,\text{km}$ there is a mélange that comprises $\sim$1200
icebergs covering 10% of the ocean surface (Figure 1a). Melting of these icebergs is the only forcing.
The cooling and freshening of the adjacent ocean cells is calculated with the three-equation formulation
(Appendix A).

The icebergs each extend over many grid cells horizontally and together act as upside-down topography
(Losch, 2008). Each iceberg is assumed to be a stationary cuboid. Although there are limitations with this
approach, it is their cumulative meltwater flux, rather than their movement, that matters most here. Further
detail and justification of our approach is given by Hughes (2022).

The icebergs follow a power-law size distribution: the number of icebergs of a given horizontal area
goes as $A^{-1.9}$ (Sulak et al., 2017), which means that smaller icebergs are more numerous than larger ones.
Horizontally, iceberg dimensions are rounded to multiples of $40\,\text{m}$ and a maximum of $320\,\text{m}\times240\,\text{m}$ is
imposed. Vertically, most icebergs have a keel depth of $30\text{–}80\,\text{m}$.
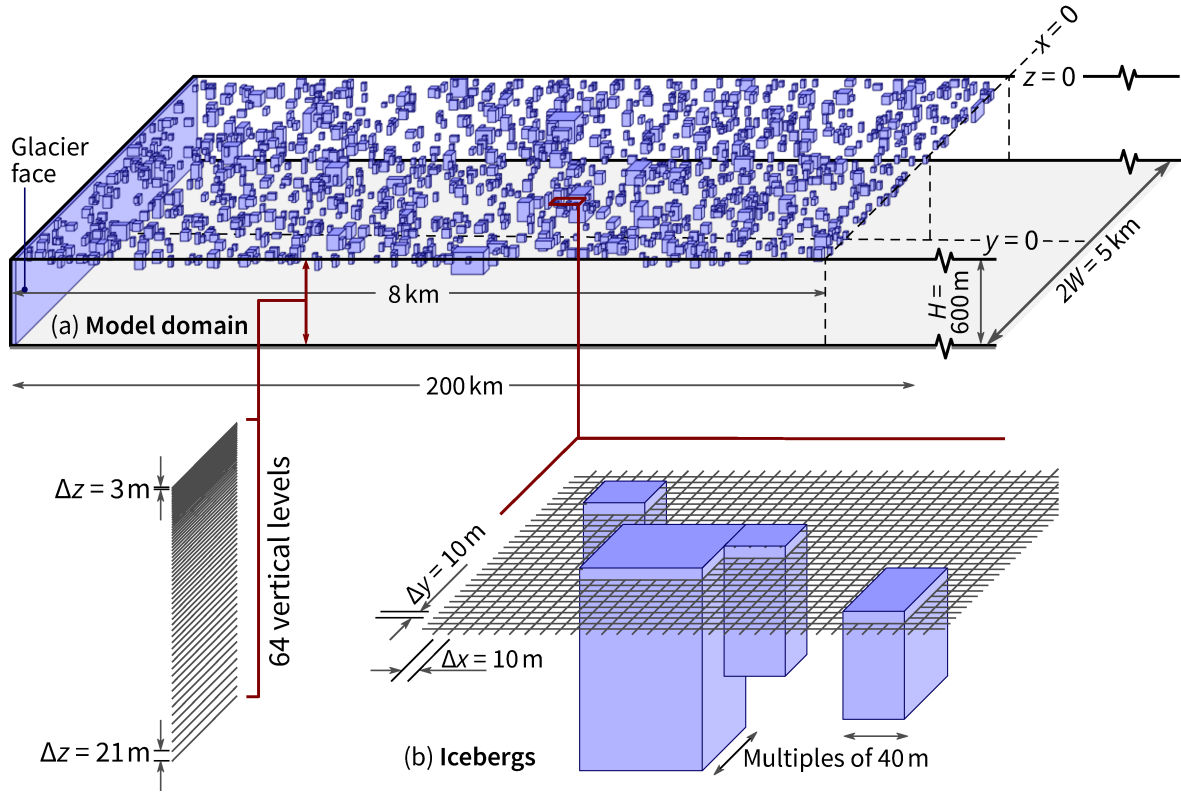
Figure 1. Numerical model setup. (a) A long rectangular fjord contains a 8 km×5 km mélange in which 10% of the surface area is covered by icebergs. Note the coordinate system with $x = 0$ at the end of the mélange, $y = 0$ in the fjord center, and $z = 0$ at the surface. (b) Volume-occupying icebergs are explicitly resolved in the model.

The ambient water initially has a constant potential temperature and linear salinity profile, and hence constant buoyancy frequency:

$$S_a(z) = 35 - \Delta S \left(1 + \frac{z}{H}\right) \tag{1}$$

$$\theta_a(z) = 2°C \tag{2}$$

$$N = \sqrt{g\beta \frac{\Delta S}{H}} \tag{3}$$

where $\Delta S = 3$ is the salinity increase between the surface and the seafloor, which is representative of values of 2–4 observed in Greenland fjords (e.g., Straneo et al., 2011; Sciascia et al., 2013), and $\beta \approx 7.8 \times 10^{-4}$ is the saline contraction coefficient. The 2°C value equates to approximately 4°C above the freezing, an

80 average thermal forcing for Greenland fjords (Wood et al., 2021). Constant temperature precludes local warming at mid depths caused by upward advection of warm water (cf. Davison et al., 2022).

The coordinate system has $x = 0$ at the end of the mélange, $y = 0$ in the center, and $z = 0$ at the surface. Within the mélange ($x < 0$), $\Delta x = \Delta y = 10$ m. Outside the mélange ($x > 0$), Δx increases 3% per cell. There are 64 vertical levels, with the highest resolution of $\Delta z = 3$ m at the surface. The time step is 2 s and

85 simulations are run in hydrostatic mode for one week. Using nonhydrostatic simulations makes negligible difference because—in a cumulative sense—meltwater is injected into a low aspect ratio layer (iceberg drafts are much smaller than the horizontal dimensions of the mélange).

Vertical mixing is parameterized with the Klymak and Legg (2010) overturning scheme with a background viscosity and diffusivity of $A_v = K_v = 10^{-4} \, \mathrm{m^2 \, s^{-1}}$. Horizontal viscosity is parameterized with a

90 Smagorinksy viscosity with the `viscC2Smag` coefficient set to 2.5 together with a background value of $A_h = 10^{-3} \, \mathrm{m^2 \, s^{-1}}$. Temperature and salinity are advected with a third-order flux limiter scheme (Hundsdorfer et al., 1995, designated as scheme 33 in the MITgcm).

The Coriolis parameter is set for 70°N ($f = 1.37 \times 10^{-4} \, \mathrm{s^{-1}}$). The channel width $2W = 0.6 L_R$, where $L_R = c_1 / f = 8.6$ km is the mode-1 internal Rossby radius. The mode-1 internal wave speed c_1 has a

95 realistic value of $1.2 \, \mathrm{m \, s^{-1}}$ (e.g., Sutherland et al., 2014)

2.2 Numerical model results

The simulated icebergs melt at 0.3–0.4 m d^{-1}, which is at the upper end of typical observed values (Enderlin and Hamilton, 2014; Enderlin et al., 2018; Schild et al., 2021). This melt creates flows of order $5 \, \mathrm{cm \, s^{-1}}$ (Figure 2). The fastest flows occur in (i) near-surface hotspots where currents are squeezed through gaps

100 between icebergs and (ii) the coastal current down-fjord at $x > 20$ km. This current hugging the 'right-hand side' is the most obvious consequence of Coriolis.

Most of the surface flow within the mélange is down-fjord as expected. The up-fjord flow in the southwest corner (Figure 2a) is perhaps unintuitive and will be explained in Section 3. When averaged over the whole mélange region, the outflow is down-fjord in the top 50 m and up-fjord below that (Figure 2e). Notably,

105 this up-fjord flow occurs despite an appreciable release of meltwater down to 100 m.

Averaged over the week-long simulation, fluxes of freshwater and heat are 110 m^3 s^{-1} and 36 TW. By the end of the week, the near-surface salinity and temperature have fallen by ∼0.3 and ∼1°C (Figure 2g–h).
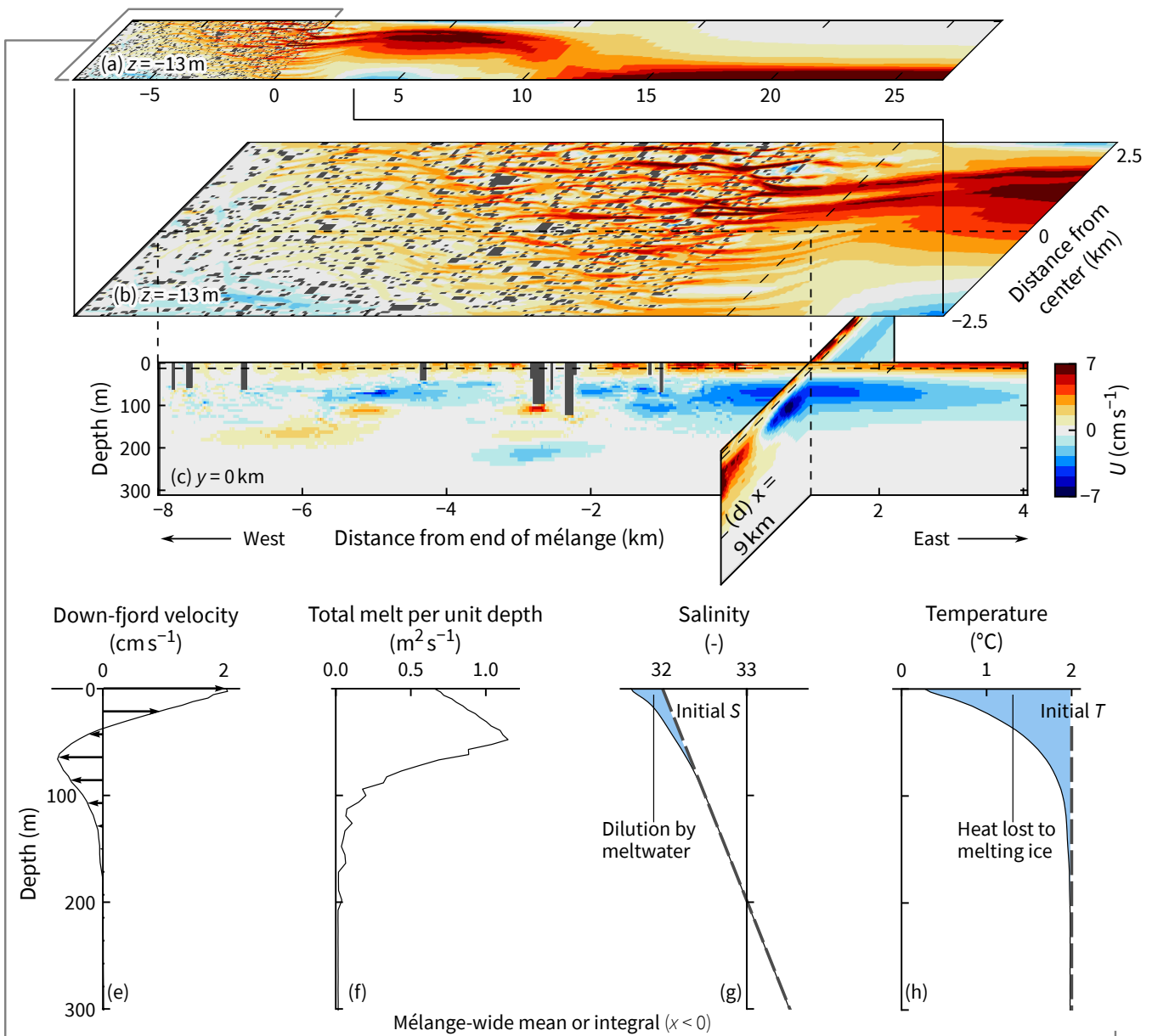
Figure 2. Dynamics of the top half of the fjord after one week of simulation. A simple description is of surface outflow in the top 50 m and inflow at 50–150 m, but Coriolis and advection complicate the picture. (a, b) A plan view. (c) An along-fjord slice. (d) A cross-fjord slice. (e–h) Properties averaged or integrated over the mélange region.

Starting from rest, the coastal current down-fjord of the mélange is the first major feature to form (Figure 3). As with the averaged flows described earlier, the coastal current flows down-fjord in the top 50 m and up-fjord over the 50–150 m range. Within 12 h, the current reaches $x = 10$ km (Figure 3b). This is too fast to be explained by advection because the currents themselves are only 1–3 cm s^{-1}. Instead, a faster wave mechanism is at play. This mechanism also explains why the coastal current extends over only a small fraction across the channel despite the channel width being only $0.6L_R$. Specifically, the decay away from the wall is faster than $\exp(-(y+W)/L_R)$ because the current has a structure comprising many modes, not just mode 1, and the higher modes have shorter Rossby radii.

Advection *is* responsible for the increasingly long channel-wide jet. Between $t = 2$ and 4 days, the easternmost end of the jet moves from $x = 2$ to 7 km (Figure 3d–e) at 3 cm s^{-1}. However, except for this jet, the evolving system that we have simulated numerically can be explained and quantified in terms of wave mechanics with an analytical model.

3 The analytical model

We will build the core of our analytical model in nine steps (Sections 3.1–3.9). Each step is based on wave mechanics in a certain scenario for which its section is named. The role of melt is added as a tenth step.

The first three sections consider the Rossby adjustment problem in a channel (also called geostrophic adjustment). We start with a two-dimensional problem of flow generated by an abrupt release of a region of high sea surface height in an open channel (Section 3.1), which is the simplest case mathematically and conceptually. We then make the geometry more realistic by closing one end (Section 3.2). Finally, we change the forcing for this closed case from abrupt to gradual (Section 3.3), which is a better analogue for a melting ice system. Note that in these Sections 3.1–3.3, 'downstream' will be to the left because it will simplify Figure 4. In later sections in which flow velocity may change sign with depth, we will use the terms 'up-fjord' and 'down-fjord'. Down-fjord will be to the right.

The middle three sections consider a different two-dimensional problem: baroclinic adjustment in the x–z domain without rotation. Again, we first consider abrupt releases in open and closed settings (Sections 3.4 and 3.5, respectively) and then look at the closed case with gradual forcing (Section 3.6)
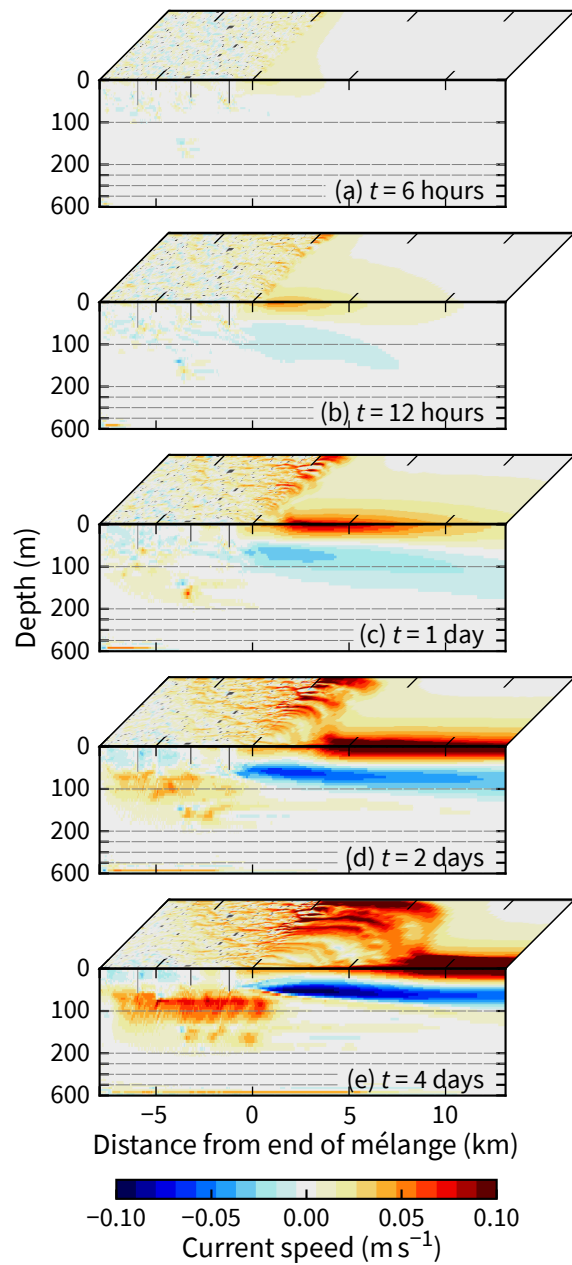
Figure 3. Development of fjord circulation from rest as depicted by vertical and horizontal slices at the southernmost side and surface, respectively ($y = -W$ and $z = 0$). The vertical axes are enlarged in the top $200\,\mathrm{m}$ where currents are fastest.

The last three sections consider the three-dimensional problem with rotation. For the third time, we start with open and closed settings with abrupt releases (Sections 3.7 and 3.8, respectively) and then the closed setting with gradual forcing (Section 3.9)

3.1 Barotropic, open channel, abrupt release, rotating

A sea surface height discontinuity in a fluid at rest is unbalanced. When released, the discontinuity generates waves and currents that restore equilibrium. Here we consider this evolution toward equilibrium for a rotating, shallow water system in a channel. The dominant signals will be Kelvin waves propagating along the boundaries and leaving behind steady boundary currents with *e*-folding scales equal to the Rossby radius. (Poincaré waves, which have a channel-wide signature, will also arise but will be much weaker.)

Consider a single discontinuity perpendicular to the channel axis (Figure 4a). Fluid initially accelerates from higher to lower sea surface height. On a time scale of $\mathscr{O}(f^{-1})$, this down-channel flow turns to the right (northern hemisphere) to form a cross-channel jet centered about the original discontinuity. On the wall where the jet converges, a Kelvin wave of elevation is generated; on the opposite wall, a Kelvin wave of depression. Over time, these two waves propagate away and leave behind two coastal currents moving in the same direction, but on opposite sides of the channel. The two currents are connected by the original cross-channel jet.

Hermann et al. (1989) give analytical expressions for this *wave-adjusted state* (i.e., the linear solution that sets up before slower advective dynamics develop). Well downstream of the initial discontinuity ($x \ll 0$), the sea surface height η, along-channel velocity u, and total down-channel flux Q are

$$\eta = \eta_0 \left[1 - \text{sech}(W/L_R) \exp(y/L_R) \right] \tag{4}$$

$$u = \eta_0 \sqrt{g/H} \, \text{sech}(W/L_R) \exp(y/L_R) \tag{5}$$

$$Q = -2\eta_0 \sqrt{gH} \tanh(W/L_R) L_R \tag{6}$$

where η_0 is half height of the initial surface discontinuity, W is the half width of the channel, and H is the depth. Hermann et al. (1989) also provide expressions for u and v close to the discontinuity, but these are more elaborate and overkill for our purposes.
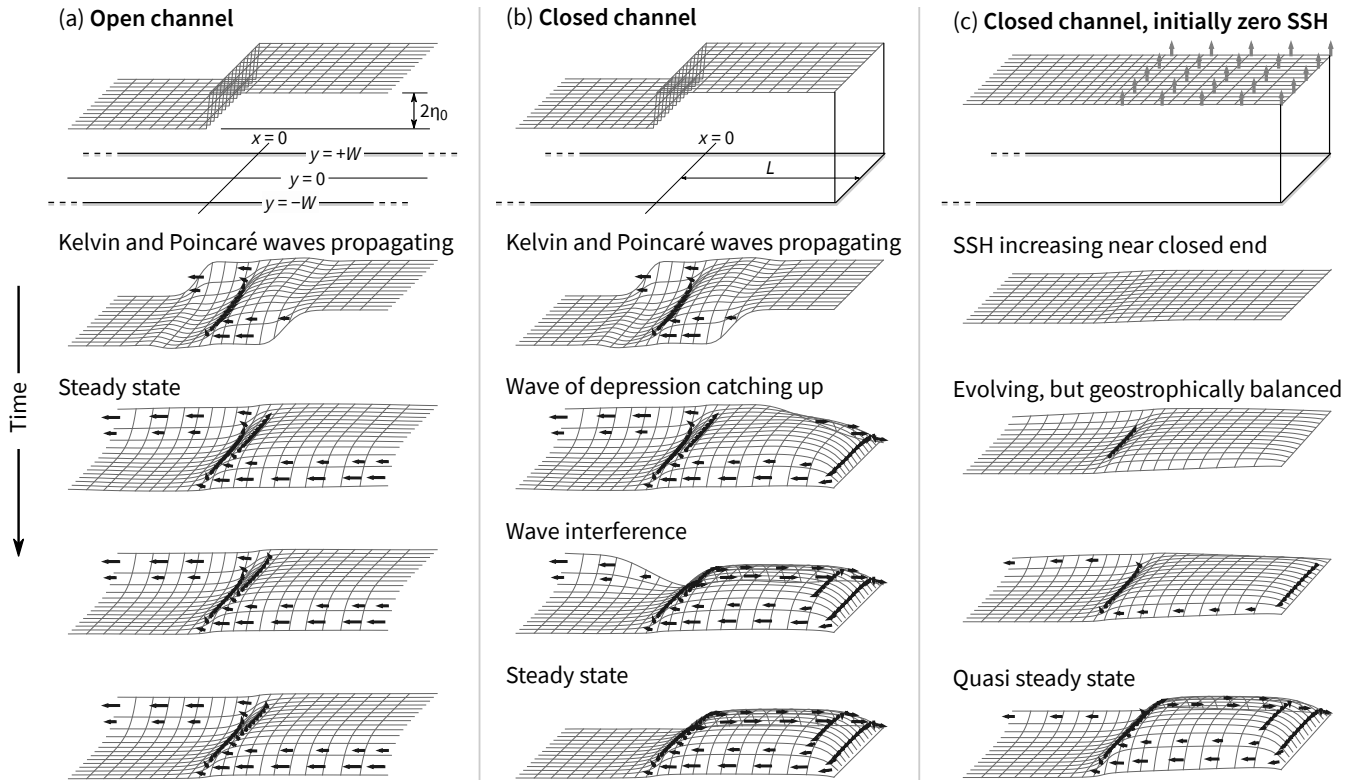
Figure 4. Rossby adjustment in a channel for three different scenarios. (a) The conventional problem with a sea surface height discontinuity in the middle of an open channel. (b) The same as panel a, but with one end of the channel closed. (c) The same as panel b, but with the sea surface being continually pushed upward from zero rather than having an initial discontinuity. Height anomalies are exaggerated in all panels.

Evaluating Eq. (5) at the boundary gives

$$u(x \ll 0, y = +W) = \eta_0 \sqrt{g/H}(1 + \tanh(W/L_R)) \tag{7}$$

For an infinitely narrow channel ($W \to 0$), the tanh term goes to zero and gives the non-rotating limit. For a wide channel ($W \gg L_R$), the tanh term goes to one and the maximum velocity is double the non-rotating limit. Regardless of channel width, the cross-channel integral of the change in potential energy is equal to the cross-channel integral of kinetic energy:

$$\int 0.5g(\eta - \eta_0)^2 \mathrm{d}y = \int 0.5u^2 H \mathrm{d}y = g\eta_0^2 L_R \tanh(W/L_R) \tag{8}$$

3.2 Barotropic, closed channel, abrupt release, rotating

If the channel is closed on the high surface end as in Figure 4b, then the wave of depression cannot propagate toward $x = \infty$. Instead, the wave propagates around the closed boundary and—after turning two corners—starts propagating in the same direction and on the same side of the channel as the wave of elevation. When this second wave passes back beyond $x = 0$, it starts to cancel the effects of the first. Hence, for $x < 0$, the down-channel flux is nonzero only between the arrival times of the two waves.

Hermann et al. (1989) did not consider this closed channel case, but it is easy to extend their formulation (quoted here as Eqs. (4)–(6)) by adding the destructive interference caused by the trailing wave. Assuming the trailing wave keeps its shape as it navigates the two corners, then the extra distance that it travels is $2L + 2W$. A time series of the flux at a given location x becomes a top-hat function with nonzero values over a period Δt where

$$\Delta t = (2L + 2W)/c \tag{9}$$

3.3 Barotropic, closed channel, gradual forcing, rotating

In Figure 4c there is no initial discontinuity. Instead the sea surface is continually pushed upward in the $x > 0$ region. This upward movement can be treated as a sum of sequential infinitesimal perturbations. Hence, the system's response can also be treated as a sum of sequential infinitesimal solutions (assuming linearity). In contrast to the abrupt closed case, η, u, and Q are nonzero in the $x < 0$ region for all values of t. Expressions for these three quantities are the same as Eqs. (4)–(6), but with

$$\eta_0 \rightarrow \frac{d\eta_0}{dt} \Delta t \tag{10}$$

where $d\eta_0/dt$ is the rate at which the sea surface is pushed upward and Δt is the wave delay from Eq. (9).

3.4 Baroclinic, open channel, abrupt release, non-rotating

We turn now to a depth dependent scenario: a non-rotating, open channel in two dimensions (x–z) with the left half having a low-density anomaly near the surface (Figure 5a). In practice, the density anomaly would vary with depth as a function of meltwater input; for now, we impose a constant anomaly in the top third of the water column.
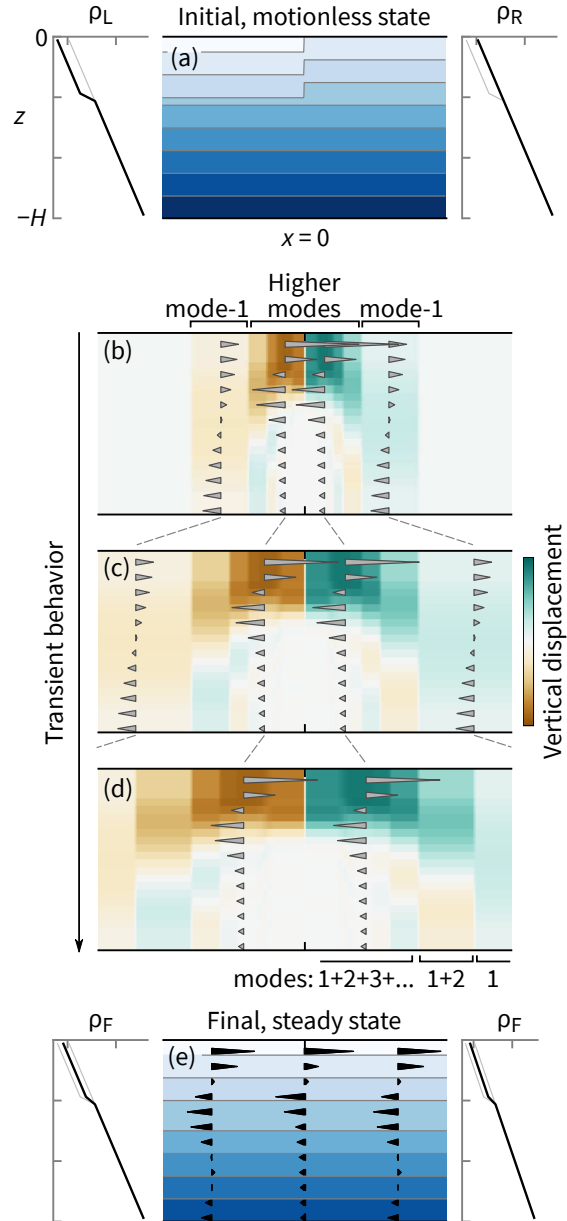
Figure 5. Baroclinic adjustment in a stratified fluid of a density anomaly near the surface of a non-rotating, open channel. (a) The initial density field. (b–d) Velocity and vertical displacement fields depicted by arrows and color shading, respectively, at three successive times. (e) The final density and velocity fields. The available potential energy in the initial, motionless state is all converted to the kinetic energy of the final, steady state. When the initial pressure anomaly is considered as a sum of internal modes, the final state—and the evolution toward it—can be predicted from the known behavior of those modes.

The density field of the final, steady state is easy to predict. Assuming no mixing occurs, the final state must contain the same fluid parcels as the initial state, but sorted vertically such that no available potential energy remains. Hence, the final density field is horizontally homogeneous (Figure 5e).

Provided the initial density anomaly is small relative to the background stratification, it will *not* slump as if it were a gravity current (e.g., Simpson, 1982). Rather, each unstable fluid parcel only travels a short vertical distance before it reaches its neutral buoyancy level. Indeed, throughout this paper we are assuming that the vertical movement of meltwater is limited by stratification and hence vertical scales are a few tens of meters at most (e.g., Huppert and Turner, 1980; Yang et al., 2023).

The rearranging of fluid parcels produces pressure perturbations that lead to internal waves with a range of mode numbers spreading out in both directions from the location of the initial density discontinuity (Figure 5b–d). For constant buoyancy frequency N and a fjord depth H, the speed of a mode-n internal wave is

$$c_n = \frac{NH}{n\pi} \tag{11}$$

Details on this expression can be found in the Appendix of Kelly et al. (2010) or Section 6.11 of Gill (1982). Throughout the main text, we are using constant stratification for its simplicity. The generalization of the analytical model to any stratification profile is described in Appendix B.

The two mode-1 waves spread out rapidly from the initial discontinuity. On the right-hand side, there is a wave with positive vertical displacements (green shades in Figure 5b–d). On the left-hand side, there is a corresponding wave with negative vertical displacements. The horizontal velocity induced by these waves is the same on either side: eastward flow near the surface and westward flow deeper down. For points between the mode-1 and mode-2 wavefronts, the velocity profile is

$$u(z) = A_{u_1} \cos\left(\frac{\pi z}{H}\right) \quad \text{for } c_2 t < |x| < c_1 t \tag{12}$$

where A_{u_1} is a Fourier coefficient to be determined later. Once the mode-2 wavefront passes the same location, its velocity superimposes on that already there. Hence,

$$u(z) = A_{u_1} \cos\left(\frac{\pi z}{H}\right) + A_{u_2} \cos\left(\frac{2\pi z}{H}\right) \quad \text{for } c_3 t < |x| < c_1 t \tag{13}$$

Similarly, the vertical displacement has both mode 1 and 2 components (see, e.g., the location labeled 'mode 1+2' in Figure 5d)

In the long-time limit, the velocity at any horizontal location is given by the generalization of Eq. (13):

$$u(z) = \sum_{n=1}^{\infty} u_n(z) = \sum_{n=1}^{\infty} A_{u_n} \cos\left(\frac{n\pi z}{H}\right) \tag{14}$$

220 In the example in Figure 5, the final velocity is 17% mode-1, 25% mode-2, 22% mode-3, 12% mode-4, and 24% higher modes.

The coefficients A_{u_n} can be derived from the initial density profiles. To start, define the density anomaly ρ' as

$$\rho'(z) = (\rho_R - \rho_L)/2 \tag{15}$$

225 where ρ_L and ρ_R are the density profiles for the initial state on the left- and right-hand sides. Then, integrate this with depth to get a hydrostatic pressure anomaly p' that is the same on both the left- and right-hand sides:

$$p'(z) = \frac{g}{\rho_0} \int_z^0 \rho'(z^*) z^* dz^* \tag{16}$$

where z^* is a dummy variable used to avoid ambiguity with the integral's lower limit. The value of $p'(z)$ is 230 zero at the surface and negative below.

Like $u(z)$, the profile $p'(z)$ can be described as a cosine series:

$$p'(z) = \frac{A_{p_0}}{2} + \sum_{n=1}^{\infty} A_{p_n} \cos\left(\frac{n\pi z}{H}\right) \tag{17}$$

where

$$A_{p_n} = \frac{2}{H} \int_{-H}^{0} p'(z) \cos\left(\frac{n\pi z}{H}\right) dz \tag{18}$$

235 Following Kelly et al. (2010), specifically their Eqs. (A12) and (A14) with $\omega = 0$, there is a simple link between the coefficients A_{u_n} and A_{p_n}:

$$A_{u_n} = CnA_{p_n}. \tag{19}$$
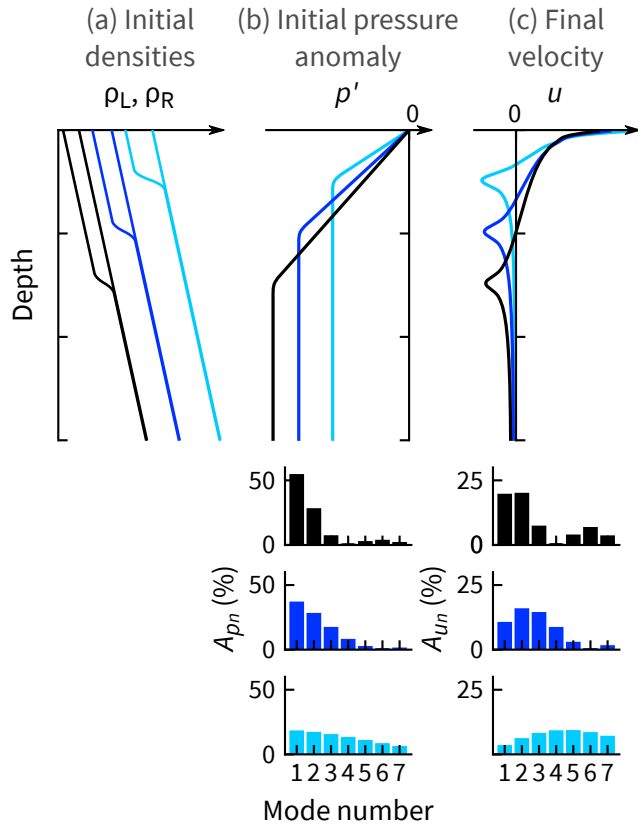
Figure 6. Examples of the link between $p'(z)$ and $u(z)$ (Eqs. (14 and (17)) for baroclinic adjustment of a non-rotating, stratified system. The black example has an initial density discontinuity that is most spread out with depth, so $p'(z)$ has lower-mode components. Hence, the associated $u(z)$ also has lower-mode components (Eq. (19)). Conversely, the light blue example is more surface-intensified and has higher-mode components. In all cases, the initial available potential energy is the same.

Therefore,

$$u(z) = C \sum_{n=1}^{\infty} n A_{p_n} \cos\left(\frac{n\pi z}{H}\right) \tag{20}$$

240 If $\rho'(z)$ is spread out with depth, then $p'(z)$ and $u(z)$ are shaped more by low mode components. If $\rho'(z)$ is surface intensified, then p' and u have higher mode components (Figure 6).

The proportionality constant C in Eq. (20) is found implicitly by equating the available potential energy E_p of the initial state to the kinetic energy E_k based on the velocity in the final state u_F, where

$$E_\mathrm{p} = \frac{g^2}{2\rho_0} \int_{-H}^{0} \frac{\rho'^2}{N^2} \, \mathrm{d}z \tag{21}$$

245
$$E_\mathrm{k} = \frac{\rho_0}{2} \int_{-H}^{0} u_F^2 \, \mathrm{d}z \tag{22}$$

Eq. (21) follows from what Kang and Fringer (2010) call APE$_3$. It is a good approximation here because vertical perturbations are small.

3.5 Baroclinic, closed channel, abrupt release, non-rotating

Baroclinic adjustment in a closed channel follows the same steps as for an open channel, but the boundary
250 breaks the symmetry and means that no steady state arises. Consider the scenario in Figure 7a of a near-surface, low-density anomaly of width L beside the closed end, where L is much smaller than the channel length. Initially, the transient behavior of the system matches that in the open channel case in Figure 5b: for each mode, two waves spread out from $x = 0$. After reaching the boundary and reflecting back to $x = 0$, the originally westward waves destructively interfere with their counterparts. Because the eastward waves had
255 an effective headstart of distance $2L$, the velocity field tends toward a series of stripes, each of width $2L$ (Figure 7b). The lower, faster modes are further to the right; the higher, slower modes trail behind. (Note the difference in presentation between Figure 5, which shows velocities as arrows, and Figure 7, which shows velocities with a red–blue colormap.)

The potential and kinetic energy in the closed case are similar to Eqs. (21) and (22) but, due to the loss
260 of symmetry, we must now compare Eqs. (23) and (24) below, which are the globally integrated potential energy at $t = 0$ and the globally integrated kinetic energy as $t \to \infty$, respectively.

With our assumption that the low-density region is small compared to the channel length, the final equilibrium state can be approximated as ρ_R, not $(\rho_L + \rho_R)/2$ as it was for the open case. Hence, the
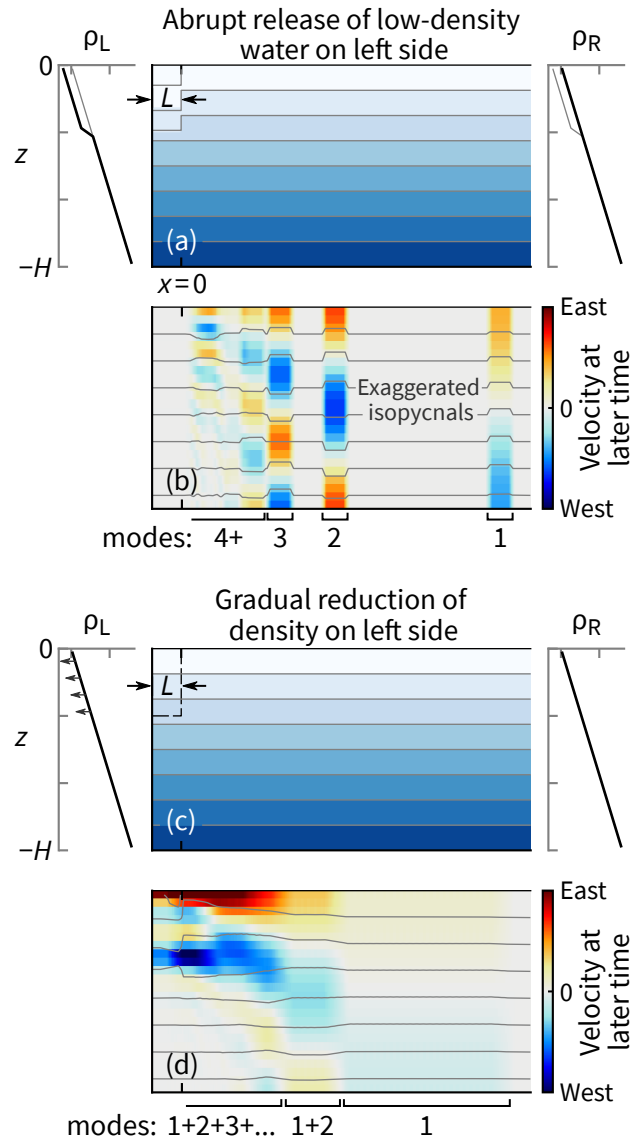
Figure 7. Baroclinic adjustment of density anomalies near the closed end of a stratified channel. (a–b) When released abruptly, the density anomaly generates two waves for each mode that spread out in each direction from $x = 0$, just as in Figure 5. However, the originally westward waves reflect at the closed end and destructively interfere with the eastward waves, except for the $2L$-wide portion of the waves that had a headstart. (c–d) If the density anomaly is gradually built up from nothing, then the outcome is the sum of sequential and infinitesimal versions of the solution in panel b.

potential energy at $t = 0$ is nonzero only in the $x < 0$ region:

$$265 \quad \int_{-L}^{\infty} E_p(t=0)\,dx = \int_{-L}^{0} E_p(t=0)\,dx = \frac{g^2 L}{\rho_0} \int_{-H}^{0} \frac{\rho'^2}{N^2}\,dz \tag{23}$$

The right-hand side is Eq. (21) multiplied by $2L$ where L comes from the x integration and the factor of 2 is associated with the change to the equilibrium state for ρ. (ρ' remains as it was defined in Eq. (15).)

The globally integrated kinetic energy expression involves u_n as defined in Eq. (14), and is best understood by considering Figure 7b. That is, the total kinetic energy is the sum of all of the $2L$-wide bands of nonzero velocity, each of which are a single mode provided they have had time to sufficiently spread out from each other:

$$\int_{-L}^{\infty} E_k(t=\infty)\,dx = \rho_0 L \sum_{n=1}^{\infty} \int_{-H}^{0} u_n^2\,dz \tag{24}$$

The kinetic energy of the system increases monotonically in time and approaches Eq. (24) as $t \to \infty$.

The velocity field at any given time, depth, and position (assuming $x > 0$) can be summarized as the total velocity induced by the eastward-propagating waves minus that of the waves that initially propagated westward and then reflected:

$$
\begin{aligned}
u(x,z,t) &= \sum_{n=1}^{n_E} u_n(z) - \sum_{n=1}^{n_W} u_n(z) \\
&= \sum_{n=n_W+1}^{n_E} u_n(z) \tag{25}
\end{aligned}
$$

The integer n_E is the maximum n for which $c_n t > x$, and similarly for n_W for $c_n t > x + 2L$.

3.6 Baroclinic, closed channel, gradual forcing, non-rotating

Consider now the same closed system, but with the low-density anomaly gradually added (Figure 7c). As in Section 3.3, we can treat this as a series of sequential and infinitesimal versions of the closed system that we just solved. For example, let the density everywhere be ρ_R at $t = 0$ and let the left side reduce at a constant rate $(\rho_L - \rho_R)/\tau$. In other words, τ is the time it would take for the left-hand side to reach ρ_L if the system were held in place so that it could not respond.

If we want to know the velocity field at any time t, then we sum a large number m (e.g., 100) solutions to the abrupt-release, closed case (Eq. (25)) that are evenly spaced in time up until t. Specifically,

$$u(x,y,z,t) = \sum_{i=1}^{m} u(x,y,z,it/m) \tag{26}$$

with the effective ρ_L reduced accordingly

$$\rho_L \to \rho_R - \frac{t}{m\tau}(\rho_R - \rho_L) \tag{27}$$

For example, if $m = 100$, then we effectively sum 100 abrupt-release cases that start at $0.00t, 0.01t, 0.02t, \ldots, 0.99t$, with each having values of $\rho_R - \rho_L$ that are scaled down by a factor of 100. Although we could also express this more formally in the limit $m \to \infty$, doing so does not provide extra insight.

With this gradual release in a stratified channel, we can start to see a resemblance between the analytical and numerical models (e.g., compare Figure 7d to Figure 3c).

3.7 Baroclinic, open channel, abrupt release, rotating

Three-dimensional baroclinic Rossby adjustment in a channel combines concepts from the x–y and x–z cases from Sections 3.1–3.6. We will use the same initial density field as in Sections 3.4–3.6 and make it constant in the across-channel direction (Figure 8a).

When the density discontinuity is released, it generates two counter-propagating families of Kelvin waves (Figure 8b): westward ones on the far side of the channel ($y = +W$) and eastward ones on the closer side ($y = -W$), just as occurred in the simpler form with barotropic waves in Figure 4a. Individually, each mode behaves like the barotropic case, except with a depth-dependent velocity and a much reduced Rossby radius. The latter for a given mode n is

$$L_{Rn} = \frac{NH}{n\pi f} \tag{28}$$

which follows from the wave speed expression in Eq. (11). Mode-1 Rossby radii are typically 5–10 km in Greenland fjords.

For regions away from the initial discontinuity, the velocity is parallel to the walls and the expression for $u(x,y,z,t)$ is separable in three dimensions. In x and z, we use the two-dimensional baroclinic solution
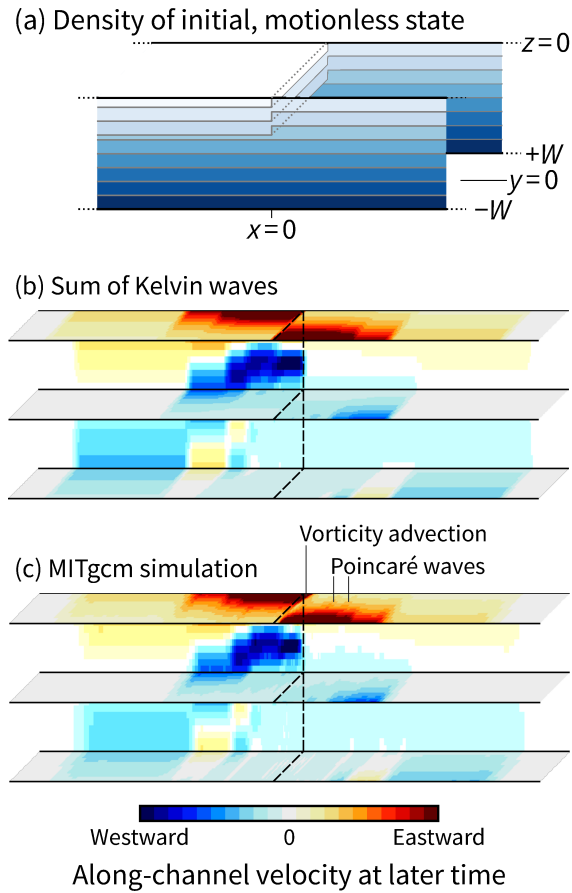
Figure 8. Baroclinic Rossby adjustment in an open-ended, stratified channel predicted by analytical and numerical models. The values of velocity are unimportant here, but the initial densities and the colormaps for panels b and c are identical. The MITgcm simulation shows two slight additions that do not arise with a semi-geostrophic approximation: advection of the discontinuity and Poincaré waves. For this particular example, the channel width is equal to the mode-1 internal Rossby radius.

310   from Section 3.4. In y, velocities decay exponentially and follow the scaling in Eq. (5). More specifically, the velocity field is

$$u(x,y,z,t) = \sum_{n=1}^{n_{\mathrm{E}}} A_{u_n} \cos\left(\frac{n\pi z}{H}\right) \mathrm{sech}(W/L_{\mathrm{R}n}) \exp(-\mathrm{sgn}(x)\,y/L_{\mathrm{R}n}) \tag{29}$$

where A_{u_n} are the velocity coefficients derived for the non-rotating x–z solution, and n_{E} is defined in Section 3.5.

315   A curious consequence of the superposition in Eq. (29) is that, at certain points, u does not decay monotonically away from the boundary. Instead, the differing scales and phases of the individual modes can lead to local maxima or minima in $u(y)$ within the channel. However, a clear example of this does not arise in Figure 8b.

To confirm that the sum of Kelvin waves is a good approximation of the true system, we test it against
320   an MITgcm simulation with the same initial conditions. (This simulation is separate to those described in Sections 2 and 4.) In Figure 8, panels b and c clearly agree, and the same is true for wider and narrower channels (not shown). The MITgcm simulation does contain additional physics—vorticity advection and Poincaré waves—but the effect on along-channel velocity is small. (See Hutter et al. (2011) for further details on Poincaré waves in channels of constant depth.)

325   Not shown in Figure 8 are the cross-channel velocities. It would be possible, albeit cumbersome, to derive $v(x,y,z,t)$ from linear wave dynamics as we have done for $u(x,y,t,z)$; the starting point would be the solution for the barotropic case (Eq. (2.22) of Hermann et al. (1989)). From the MITgcm simulations, we find as expected that v (not shown) peaks near $x = 0$, goes to zero at $|x| \gg 0$, and is negative at the surface: water flows from $y = +W$ to $-W$. A counterflow from $-W$ to $+W$ occurs at the depth $z = -H/3$
330   where the discontinuity goes to zero.

3.8   Baroclinic, closed channel, abrupt release, rotating

In a closed channel, the baroclinic Kelvin waves propagating toward the closed end start at $(x,y) = (0, +W)$, travel a distance L westward, turn a corner, travel a distance $2W$ southward, turn another corner, and travel a distance L eastward to arrive at $(0, -W)$. Thereafter, they destructively interfere with their counterparts.
335   This is the same argument as in the barotropic case in Section 3.2. Ultimately, Eq. (25) can be applied here to the three-dimensional channel with n_{W} now being the maximum value of n for which $c_n t > x + 2L + 2W$.
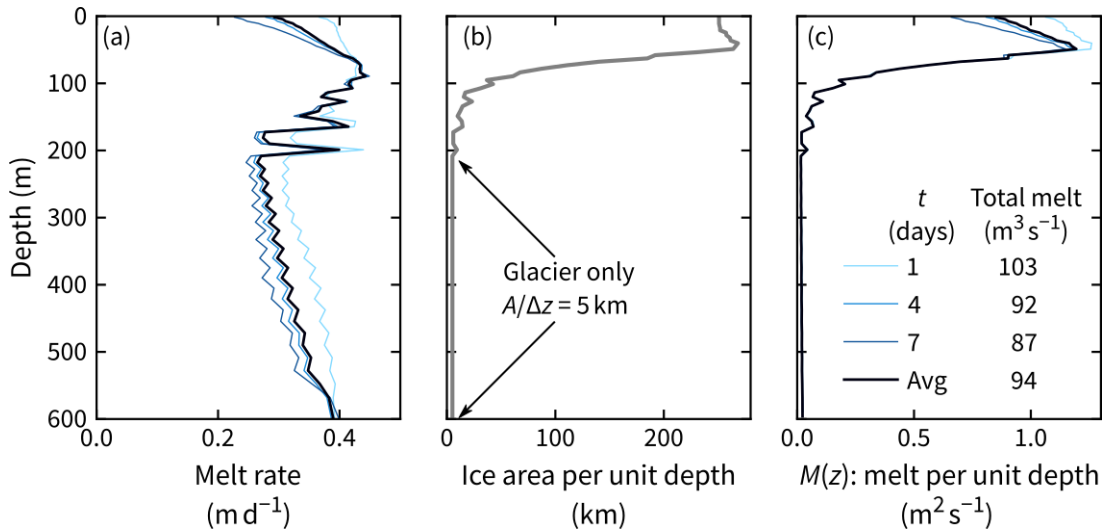
Figure 9. Iceberg (and glacier) melt in the numerical model. (a) Melt rates are $\sim$0.3 m d^{-1} and decrease over time, especially near the surface, as the surrounding water cools. (b) Total ice surface area in units equivalent to a width. (c) The product of panels a and b in units that are suitable for the analytical model.

3.9 Baroclinic, closed channel, gradual forcing, rotating

The final step before incorporating melt is anticlimactic because the hard work has been done. To adapt the closed, abrupt release case from the previous section to the gradual release case, we simply repeat the methodology described by Eqs. (26) and (27).

3.10 Incorporating ice melt into the analytical model

In Sections 3.4–3.9, there is a low-density anomaly in the upper third of the water column in the $x < 0$ region that either exists at $t = 0$ or develops gradually as t increases. The numerical model from Section 2 is set up similarly in that meltwater is continually injected into the $x < 0$ region.

In a glacier context, melt rates are often discussed in velocity units, with a convenient unit being m d^{-1} as in Figure 9a. In iceberg-choked fjords, the total surface area of ice in contact with water can be an order of magnitude larger (Sulak et al., 2017). Indeed, expressing this surface area *per unit depth* gives a quantity that is equivalent to a glacier width, but much bigger, especially near the surface (e.g, $\sim$200 km in Figure 9b).

350   Let $M(z)$ denote the total, time-averaged meltwater input per unit depth with units of $\mathrm{m^2\,s^{-1}}$. (The depth integral of $M(z)$ is the volume flux of meltwater.) Many remote sensing studies provide methods to estimate $M(z)$ from either observed rates of change of iceberg freeboard or parameterizations of melting (Enderlin and Hamilton, 2014; Enderlin et al., 2018; Moon et al., 2018; Moyer et al., 2019; Rezvanbehbahani et al., 2020). We, however, have the benefit of the exact value of $M(z)$ being a model output, so we will use this

355 hereafter (Figure 9c).

    To use the analytical model, we need an expression for $\rho_L(z)$ that plugs into Eq. (27). We start with meltwater's properties (see, e.g., Jenkins, 1999):

$$S = 0 \tag{30}$$

$$\theta_{\text{eff}} \approx -\frac{L}{c} + \frac{c_i}{c}\theta_i \tag{31}$$

360 where θ_{eff} is the effective potential temperature of meltwater, θ_i is the ice temperature, L is the latent heat of fusion, and c_i and c are the specific heat capacities of ice and water, respectively. The value of θ_{eff} is approximately $-85°\mathrm{C}$ and is dominated by the first term, which accounts for the heat extracted from the water to induce the phase change; the second term accounts for sensible heating of the ice to its freezing point.

365   In Section 3.6, we defined the profile ρ_L together with the time scale τ that defined how long it took for the left side to reduce from ρ_R to ρ_L at a constant rate. Here, we set a somewhat arbitrary value for τ of 7 days and calculate ρ_L at this time based on the meltwater input. The value of τ later cancels when used in Eq. (27).

    At time τ, the volume of meltwater per unit depth added over the mélange will have reached $\Delta A(z) =$

370 $M(z)\tau$. If the fjord did not respond dynamically to this meltwater, then the average properties throughout the mélange region—based on weighted averages of the ambient water and meltwater—would become

$$S_L = \frac{A_0 S_R}{A_0 + \Delta A} \tag{32}$$

$$\theta_L = \frac{A_0 \theta_R + \Delta A \theta_{\text{eff}}}{A_0 + \Delta A} \tag{33}$$

$$\rho_L = \rho(S_L, \theta_L) \tag{34}$$

375 where S_R and θ_R are the initial salinity and potential temperature profiles, and $A_0(z) = 2WL\phi(z)$ is the mélange area scaled by the water fraction $\phi(z)$. In our numerical model, we have $\phi = 0.9$ at the surface because 10% of the surface is covered by icebergs.

4   Comparing the analytical and numerical models

The analytical model should work in regions governed by linear wave dynamics; it is not expected to work
380 where advection dominates (e.g., at $x \lesssim 15\,\text{km}$ in Figure 2a). We will start by testing it at $x = 20\,\text{km}$ by comparing its prediction to the numerical model from Section 2.

Consider first the cross-channel structure. At $t = 1$ day, the analytical model correctly predicts that the flow (i) has peak velocities of $1\,\text{cm}\,\text{s}^{-1}$, (ii) has a zero-crossing at $100\,\text{m}$ depth, and (iii) has a decay scale comparable to the width of the channel (Figure 10a–b). Also correctly predicted, albeit a minor detail, is
385 the small outflowing patch centred near $350\,\text{m}$ depth. Later, at $t = 3$ and 7 days (Figure 10c–f), there is a larger contribution from higher-modes, and the flows are consequently more concentrated in the top $100\,\text{m}$. The analytical model still predicts well the velocity fields at both of these times.

When compared carefully, the analytical model slightly overpredicts the velocities. This is best quantified by evaluating the total outflow Q_{out}, which is the area integral of all outflowing fluid:

$$390 \quad Q_{out} = \int_{u>0} u\,dy\,dz \tag{35}$$

Between 3 and 7 days (once a quasi-steady state is approached), the analytical model overpredicts Q_{out} at $x = 20\,\text{km}$ by 25% (compare the grey and black lines in Figure 11a). At $t = 7$ days, the analytical model predicts that Q_{out} is approximately independent of distance from the melange—at least for $x < 100\,\text{km}$ (Figure 11b). The same approximate independence arises in the numerical model results, except in the
395 aforementioned advective region of $x < 15\,\text{km}$.

Given the number of approximations and assumptions that go into the analytical model, we deem that it agrees reasonably well with the numerical model. One notable assumption not yet discussed is that the icebergs have no dynamical effect as obstacles. In the numerical model, the icebergs are stationary and induce drag on near-surface flows (Hughes, 2022), which includes the set of Kelvin waves that initially
400 travel westward from $x = 0$ and then anti-clockwise around the fjord boundary.
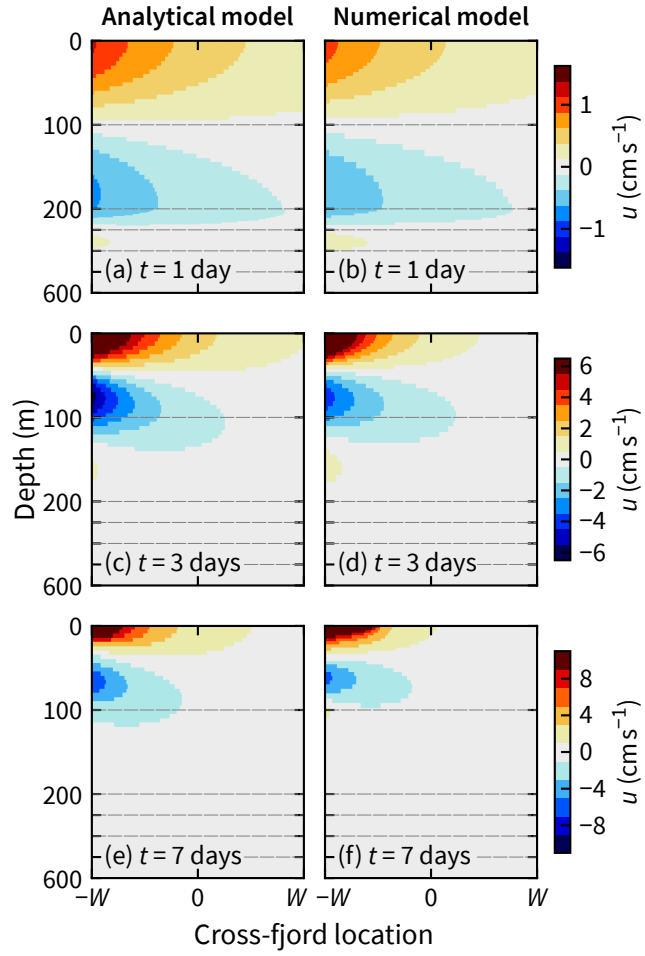
Figure 10. Snapshots at $x = 20\,\text{km}$ after 1, 3, and 7 days show that the analytical predictions in the left column agree with the numerically simulated velocities in the right column. Note that the color limits increase from the top to bottom and that the vertical axes are enlarged in the top 200 m as in Figure 3.

To further test the analytical model, we repeat the Q_{out} comparisons for two other model scenarios. The first scenario has stronger stratification: the salinity difference between the surface and seafloor is doubled (ΔS in Eq. (1) is 6, not 3). The second scenario has weaker melt rates: the turbulent transfer coefficients for heat and salt are four times smaller than the default case (γ_T and γ_S in Eqs. (A3) and (A4)). In these two further tests, the analytical model still predicts well the numerically simulated flow both in terms of total outflow (Figure 11) and cross-channel structure (not shown). In fact, the agreement is better in these two
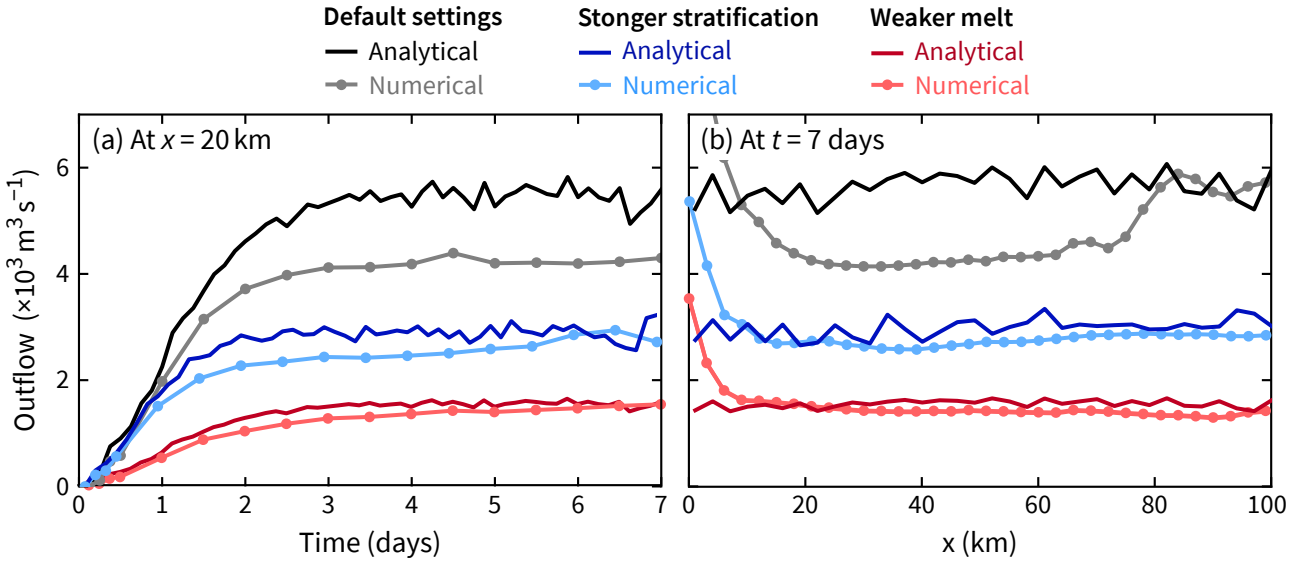
Figure 11. The analytical model predicts well the outflow (Eq. (35)) for three different scenarios. (a) Outflow at a specific location: 20 km. (b) Outflow at a specific time: 7 days. The discrepancies are discussed in the main text.

scenarios compared to the default settings because the relative role of linear wave dynamics (compared to nonlinear advection) is larger when the outflow is weaker or the stratification is stronger.

Three comparisons is, of course, far from an exhaustive test of the plausible parameter space. Yet given
410   the agreement in all cases, there is no reason not to trust the analytical model.

5   Discussion

5.1   What parameters does melt-induced circulation depend on?

There are several obvious ways that melt-induced fjord circulation could increase: warmer ambient water, a larger mélange, or enhanced turbulent transfer at the ice–ocean interface.
415   To examine these dependencies in detail—and the less intuitive role of stratification—we undertake a parameter space study using the analytical model to predict $Q_{out}(x = 20\,\text{km})$ under a range of conditions. For simplicity, we will change one parameter at a time; all others will have the default values used previously ($L = 8000\,\text{m}$, $2W = 5000\,\text{m}$, $H = 600\,\text{m}$, $\Delta S = 3$, and $\theta_a = 2°\text{C}$). We will also assume a total
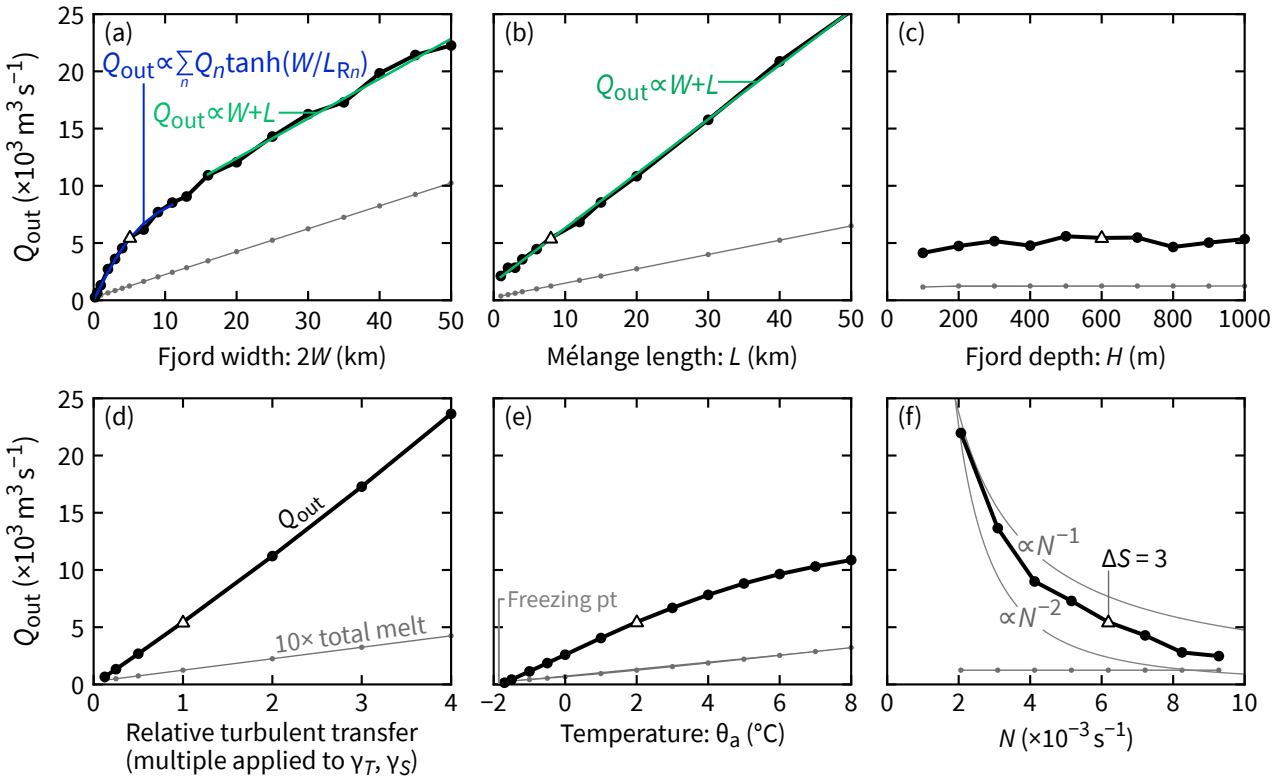
Figure 12. Predictions from the analytical model of how outflow (Q_{out}) depends on geometrical parameters, ice–ocean turbulent transfer, and water column properties. In each panel, single quantity is varied; the others are fixed at the values highlighted by the triangles in the other five panels. Note how the total meltwater flux, which is shown for reference, is multiplied by a factor of ten to make it visible on the same scale.

melt rate profile similar to that in Figure 9c. Specifically,

$$M(z) = 2.5 \times 10^{-8} WL \left(1 + \tanh \left(\frac{z + 100}{25} \right) \right) \tag{36}$$

where $100\,\mathrm{m}$ is the depth at which $M(z)$ drops to half of its surface maximum and $25\,\mathrm{m}$ is a vertical length scale. For the default fjord geometry, $M(z=0) = 1\,\mathrm{m}^2\,\mathrm{s}^{-1}$.

Q_{out} increases monotonically with channel width (Figure 12a). For narrower channels there is a dependence on $\sum_n Q_n \tanh(W/L_{Rn})$ where Q_n are coefficients. This follows from generalizing Eq. (6) to the baroclinic case involving a sum of modes, each with their own internal Rossby radius L_{Rn}. (Presumably the coefficients Q_n could be derived from the analytical model, but that is not our goal here.) For wider channels $Q_{out} \propto W + L$ because the distance $2L + 2W$ is the distance a Kelvin wave travels around the

perimeter of the fjord to move from $(0, +W)$ to $(0, -W)$, and this distance governs the total flux (see Sections 3.2 and 3.8). For the same reason, a $Q_{\text{out}} \propto W + L$ scaling also arises when varying L while keeping W constant (Figure 12b). The other geometrical parameter—fjord depth H—has no significant effect on Q_{out} (Figure 12c).

If the fjord geometry is fixed, but the ice–ocean interface conditions are changed, then Q_{out} scales approximately linearly with the meltwater flux. In Figure 12d, we alter the ice–ocean turbulent transfer coefficients γ_T and γ_S (see Appendix A). In Figure 12e, we alter the ambient temperature. In both cases, linearity dominates; slight deviations from this arise from nonlinearities in the equation of state and the melt rate derived from the three-equation formulation. Note, however, that for this analysis we assumed a fixed ambient velocity of $0.04 \, \text{m s}^{-1}$ (see Appendix A). Different melt formulations (e.g., Greisman, 1979; Magorrian and Wells, 2016; Malyarenko et al., 2020) may lead to different dependencies for Q_{out}, but we do not investigate these here.

Q_{out} vs water column stratification N is the scaling needing the most steps to explain. First, recall the open channel, non-rotating system from Section 3.4. There, u and hence Q_{out} are $\propto N^{-1}$ because $E_p = E_k \propto N^{-2}$ (Eq. (21)). However, $Q_{\text{out}} \propto N^{-2}$ for the equivalent closed, gradual-release system (Section 3.6). The additional factor of N^{-1} arises because internal wave speed $c \propto N$ (Eq. (11)). Specifically, recall Figure 7 in which the gradual-release case was described as the sum of sequential versions of the abrupt-release case, with the latter consisting of $2L$-wide bands of nonzero velocity. These bands move and separate at a rate $\propto N$, and so the magnitude of their sum is $\propto N^{-1}$. This already elaborate explanation is further complicated by rotation because the internal Rossby radii $L_{Rn} = c_n / f \propto N/n$. With increasing L_{Rn}, flow occupies a wider portion of the channel and hence Q_{out} increases. Ultimately, in the full system, Q_{out} has a scaling that tends to fall between N^{-1} and N^{-2} (Figure 12f).

All panels in Figure 12 include a line showing the total meltwater flux. In many cases, Q_{out} is $\sim$50 times larger than the meltwater flux, but in some cases the ratio is as large as 200 (small L or small N) or as small as 20 (large W or large N).

5.2 The value of simple scaling laws in Greenland fjords

An ambitious goal for our analytical model would be to make large-scale predictions like those that exist for the role of subglacial discharge. These start with classic buoyant plume theory (Morton et al., 1956), extend

it to a salinity-stratified system, and then apply it on a large scale. For example, Slater et al. (2016) show that outflow in a fjord is proportional to $Q_{\text{sg}}^{3/4}/N^{5/8}$, where Q_{sg} is the subglacial discharge rate. Slater et al. (2022) applies this scaling to more than 100 fjords around Greenland to predict that a total of $20\,000\,\text{m}^3\,\text{s}^{-1}$ of meltwater discharge gets amplified by a factor of $\sim$50 due to entrainment and that the outflow is spread over the top $\sim$200 m.

A more immediate goal is to help interpret observations or numerical models for specific settings. For example, as part of ongoing related work, we are analyzing multi-year simulations of Sermilik Fjord with and without icebergs (using a setup like Davison et al. (2020), but with seasonal variability included). Iceberg effects are isolated by looking at the difference between the two simulations. One plausible but counter-intuitive hypothesis stemming from the analytical model is that melt-induced circulation will be larger in winter than in summer. Why? Because in winter the water column is less stratified (hence larger iceberg-melt-induced outflow) and this may overcome the effect of slower melting in cooler waters.

5.3   Next steps

The analytical model is built on linear wave dynamics; nonlinear advection and instabilities are ignored. In parts of the domain, this can quickly become a limitation. In the numerical model we saw advection dominating in the $0 < x < 10\,\text{km}$ region after only one week of spin up (Figure 2a). In principle, it may be possible to extend the analytical model to predict this advective component. The approach would follow Hermann et al. (1989) from who we borrowed the analytical expressions for the barotropic wave-adjusted state in Section 3.1. For Hermann et al., the wave-adjusted state was merely the starting point for predicting the slower advective dynamics. In our *baroclinic* setting, however, the math would quickly become cumbersome.

Instead, it makes more sense to simply ask whether the analytical model would remain skillful after several months? Without running simulations to properly answer this, our best guess follows from Carroll et al. (2017) who simulated circulation induced by subglacial discharge on time scales of months. Their Figures 2 and 3 imply that spin up of the linear circulation (i.e., boundary currents) happens within the first five days. Thereafter, eddies form via instabilities and advection, especially in the wider channels. Nevertheless, their outflow metric seems mostly unaffected by these nonlinearities.

Other obvious uncertainties surround whether the analytical model still works in fjords that feature sills or have realistic coastlines, whether it remains useful in the presence of competing forcings such as shelf waves and subglacial discharge, and how it should be adapted for the case where there is not a convenient demarcation of mélange and open water, but rather where iceberg concentration varies along the fjord.

6   Conclusion

The analytical model involved many steps. A summarizing example helps bring all of these steps together.

The continual input of meltwater generates a continual fjord response. Discretizing the problem in time makes this response easier to understand. In Figure 13, we divide the problem into 100 pieces: 1% of the meltwater is released at $t = 0.00t_0$, another 1% is released at $t = 0.01t_0$, and so on up to $t = 0.99t_0$. The circulation at $t = t_0$ is the sum of these (Figure 13b).

For the response to the last 1% released at $t = 0.99t_0$, we see the lower modes move away quickly from $x = 0$ with the higher modes trailing behind (Figure 13c). In front of the mode-1 wavefronts on each side of the fjord, velocities are zero. Behind the mode-1 wavefronts, but in front of the mode-2 wavefronts, the velocities are down-fjord in the top half and up-fjord in the bottom half. These velocities decay exponentially from the wall but, being mode-1, they extend a reasonable distance. Wavefronts for the higher modes trail behind and their associated velocities decay rapidly with distance from the wall. The same general velocity structure is present for the case with meltwater released at $t = 0.98t_0$, except that the mode-1 wavefront on the far side has turned the corner (Figure 13d).

For the $t = 0.95t_0$ case (Figure 13e), the mode-1 wave that originated on the far side travels around the fjord perimeter and starts to interfere with the velocity field generated by the other set of Kelvin waves. The mode-2 wave does the same in the $t = 0.90t_0$ case (Figure 13f). With enough time, this interference occurs for all modes. Indeed, for the $t = 0.00t_0$ case, the velocity field shown in Figure 13g is zero for $x > 0$. This motionless region therefore has no influence on the total velocity field in Figure 13b.

Figure 13 implicitly illustrates that, down-fjord of $x = 0$, melt-induced fjord circulation reaches a quasi-steady state in which it is only responding to the 'recent' input of meltwater, with 'recent' linked to the time it takes for the relevant modes (say modes 1 through 10) to travel around the boundary. For most most Greenland fjords, this will be only a few days.
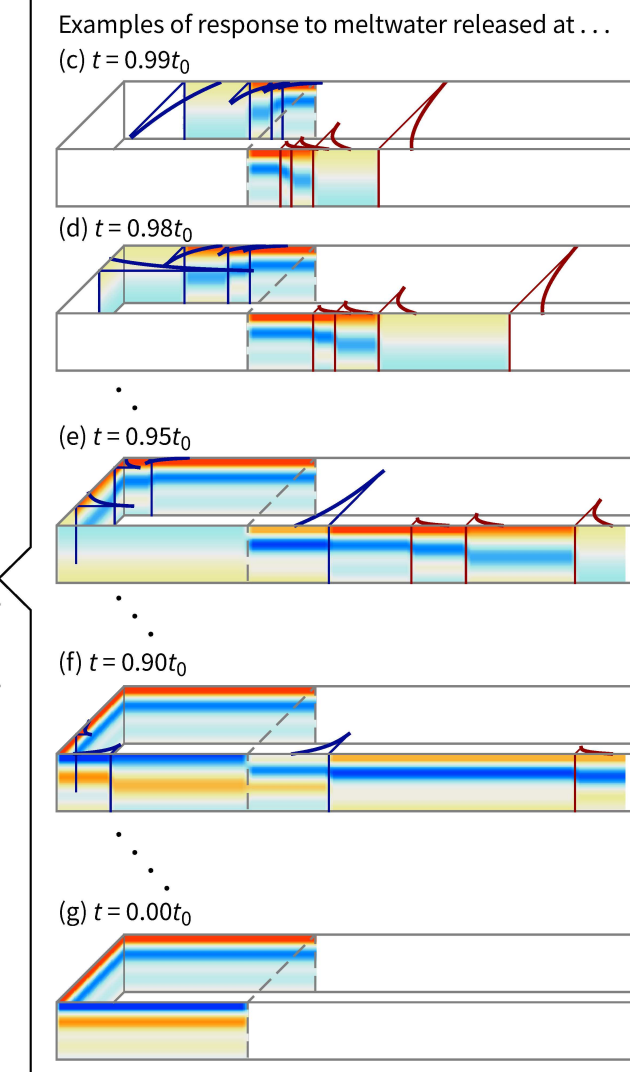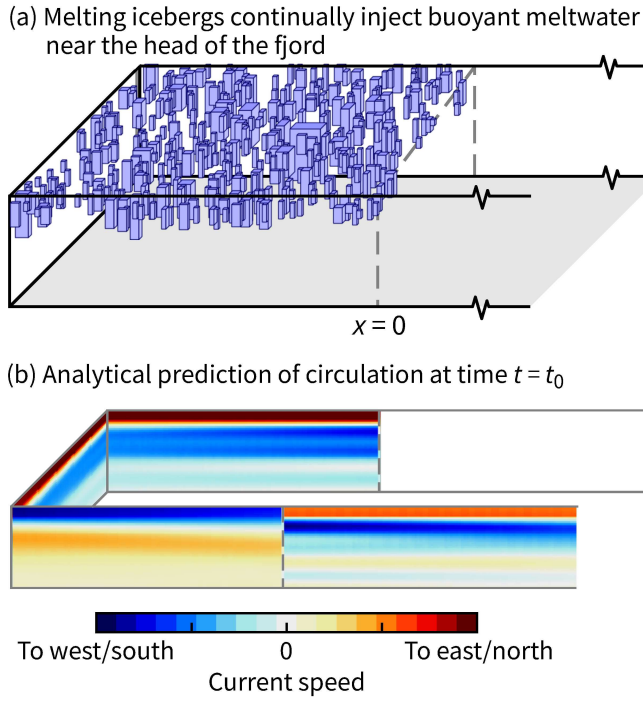
Figure 13. Summary of the analytical model. To predict the total fjord circulation at a given time $t = t_0$ as in panel b, we approximate the continual forcing as, say, 100 sequential, abrupt release cases, examples of which are shown in panels c–g. See Section 6 for a complete description. For clarity, velocities are shown only at the fjord edges and only the lowest four modes are considered. Color scales in panels c–g are the same, but they are different to that in panel b.

510   Ultimately, the analytical model—and the scalings that follow from it (Section 5.2)—can help to tame the daunting problem of predicting the dynamics of fjords that are subject to numerous forcings, of which iceberg melt is only one. Of course, there is still much to do in extending our analytical model to one that is directly applicable to a realistic fjord. But we have taken the first steps to predicting flows induced by iceberg melt that could be applied to fjords across Greenland.

Appendix A: Ice–ocean thermodynamics

In our simulations, icebergs produce meltwater through only subsurface melting; wave erosion and melting at the ice–air interfaces are ignored. Thermodynamics at all ice–ocean interfaces are treated with the three-equation formulation, and the same velocity-dependent turbulent transfer coefficients are used for the vertical sides and the basal face. Specifically, we adapt the 'icefront' package implementation from Xu et al. (2012). Turbulent heat fluxes to the ice–ocean interface are

$$\text{heat transfer } [\text{W m}^{-2}] = \rho c_\text{p} \gamma_T |\mathbf{u}| \Delta T \tag{A1}$$

$$\text{salt transfer } [\text{m s}^{-1}] = \gamma_S |\mathbf{u}| \Delta S \tag{A2}$$

where ΔT is the difference between the temperature *at* the ice–ocean interface and the temperature in the adjacent ocean cell, and similarly for ΔS. The interface conditions come from the solution to the three-equation formulation. The transfer coefficients for heat and salt in units of m s^{-1} are $\gamma_T |\mathbf{u}|$ and $\gamma_S |\mathbf{u}|$ where

$$\gamma_T = 4.4 \times 10^{-3} \tag{A3}$$

$$\gamma_S = 1.24 \times 10^{-4} \tag{A4}$$

$$|\mathbf{u}| = \min\left(\sqrt{u^2 + v^2 + w^2}, 0.04\,\text{m s}^{-1}\right) \tag{A5}$$

The values of γ_T and γ_S are far from well constrained; the decimal places are shown only to help preserve a link to previous studies that used $\gamma_T = 1.1 \times 10^{-3}$ and $\gamma_S = 3.1 \times 10^{-5}$ (e.g., Xu et al., 2012; Sciascia et al., 2013). Observations suggest these values are too low at vertical or near-vertical ice faces in Greenland (Jackson et al., 2020; Schulz et al., 2022). We have increased γ_T and γ_S by a factor of four following the suggestion of Jackson et al. (2020, 2022)[1] based on their scenario in which a resolved horizontal velocity is incorporated into the calculation of the transfer coefficients (rather than just vertical velocity). In our case, $|\mathbf{u}|$ values are calculated in the cells adjacent to ice–water interfaces. At each interface, two of the three velocity components will be nonzero. For example, $v \neq 0$ and $w \neq 0$ for an ice face in the y–z plane. The $0.04\,\text{m s}^{-1}$ lower limit follows Slater et al. (2015) and is intended to represent unresolved melt-driven convection.

---

[1]Jackson et al. (2020) and some other studies define the conventional values of γ_T and γ_S in an alternate way. Namely, $\gamma_T = \sqrt{C_\text{d}}\Gamma_T$ and $\gamma_S = \sqrt{C_\text{d}}\Gamma_S$ where $C_\text{d} = 2.5 \times 10^{-3}$, $\Gamma_T = 2.2 \times 10^{-2}$, and $\Gamma_S = 6.2 \times 10^{-4}$.

Appendix B: Extension to arbitrary stratification

Conceptually, the analytically model does not change if the reference density is nonlinear. The only difference is that mode shapes and internal wave speeds need to be calculated numerically with matrix methods.

Mode shapes for vertical velocity, denoted ϕ_n^w, are the eigenvectors of the following equation:

$$\frac{\partial^2}{\partial z^2}\phi_n^w + \frac{N^2}{c_n^2}\phi_n^w = 0 \tag{B1}$$

with boundary conditions requiring that $\phi_n^w = 0$ at the surface and seafloor. The internal wave speeds c_n are derived from the eigenvalues. We are interested in the horizontal velocity mode shapes, which we denote ϕ_n without a superscript:

$$\phi_n = \frac{\partial \phi_n^w}{\partial z} \tag{B2}$$

It is easy to confirm that $\phi_n = \cos(n\pi z/H)$ and $c_n = NH/n\pi$ are eigensolutions to the above set of equations if N is constant. Extending the analytical model to nonlinear stratification simply involves replacing all appearances of $\cos(n\pi z/H)$ and $NH/n\pi$ with ϕ_n and c_n, respectively.

Code availability. The archive at doi.org/10.5281/zenodo.8339482 includes (i) the analytical model written in Python, (ii) all the code and configuration files necessary to recreate the MITgcm results, and (iii) snapshots of these results in netCDF format. The analytical model is also available at github.com/hugke729/IcebergMeltCirculation.

Competing interests. The author declares that they have no conflict of interest.

Acknowledgements. Thank you to the two anonymous reviewers that helped clarify and improve several aspects of this paper.

Financial support. This work was funded by the Heising-Simons Foundation (grant # 2019-1159) as part of the

560 program 'Eyes at the front: a megasite project at Helheim Glacier.' The numerical simulations were run on the Expanse

system at the San Diego Supercomputer Center through allocation EES220032 from the Advanced Cyberinfrastructure

Coordination Ecosystem: Services and Support (ACCESS) program, which is supported by National Science

Foundation grants #2138259, #2138286, #2138307, #2137603, and #2138296.

References

Adcroft, A., Hill, C., Campin, J.-M., Marshall, J., and Heimbach, P.: Overview of the formulation and numerics of the MIT GCM, in: Proceedings of the ECMWF seminar series on Numerical Methods, Recent developments in numerical methods for atmosphere and ocean modelling, pp. 139–149, 2004.

Beaird, N., Straneo, F., and Jenkins, W.: Characteristics of meltwater export from Jakobshavn Isbræ and Ilulissat Icefjord, Ann. Glaciol., 58, 107–117, https://doi.org/10.1017/aog.2017.19, 2017.

Bendtsen, J., Mortensen, J., and Rysgaard, S.: Modelling subglacial discharge and its influence on ocean heat transport in Arctic fjords, Ocean Dyn., 65, 1535–1546, https://doi.org/10.1007/s10236-015-0883-1, 2015.

Carroll, D., Sutherland, D. A., Shroyer, E. L., Nash, J. D., Catania, G. A., and Stearns, L. A.: Modeling turbulent subglacial meltwater plumes: Implications for fjord-scale buoyancy-driven circulation, J. Phys. Oceanogr., 45, 2169–2185, https://doi.org/10.1175/JPO-D-15-0033.1, 2015.

Carroll, D., Sutherland, D. A., Shroyer, E. L., Nash, J. D., Catania, G. A., and Stearns, L. A.: Subglacial discharge-driven renewal of tidewater glacier fjords, J. Geophys. Res. Oceans, 122, 6611–6629, https://doi.org/10.1002/2017JC012962, 2017.

Cowton, T., Slater, D., Sole, A., Goldberg, D., and Nienow, P.: Modeling the impact of glacial runoff on fjord circulation and submarine melt rate using a new subgrid-scale parameterization for glacial plumes, J. Geophys. Res. Oceans, 120, 796–812, https://doi.org/10.1002/2014JC010324, 2015.

Davison, B. J., Cowton, T. R., Cottier, F. R., and Sole, A. J.: Iceberg melting substantially modifies oceanic heat flux towards a major Greenlandic tidewater glacier, Nat. Commun., 11, 5983, https://doi.org/10.1038/s41467-020-19805-7, 2020.

Davison, B. J., Cowton, T., Sole, A., Cottier, F., and Nienow, P.: Modelling the effect of submarine iceberg melting on glacier-adjacent water properties, The Cryosphere, 16, 1181–1196, https://doi.org/10.5194/tc-16-1181-2022, 2022.

De Andrés, E., Slater, D. A., Straneo, F., Otero, J., Das, S., and Navarro, F.: Surface emergence of glacial plumes determined by fjord stratification, The Cryosphere, 14, 1951–1969, https://doi.org/10.5194/tc-14-1951-2020, 2020.

Enderlin, E. and Hamilton, G.: Estimates of iceberg submarine melting from high-resolution digital elevation models: application to Sermilik Fjord, East Greenland, J. Glaciol., 60, 1084–1092, https://doi.org/10.3189/2014JoG14J085, 2014.

Enderlin, E. M., Hamilton, G. S., Straneo, F., and Sutherland, D. A.: Iceberg meltwater fluxes dominate the freshwater budget in Greenland's iceberg-congested glacial fjords, Geophys. Res. Lett., 43, 11 287–11 294, https://doi.org/10.1002/2016GL070718, 2016.

Enderlin, E. M., Carrigan, C. J., Kochtitzky, W. H., Cuadros, A., Moon, T., and Hamilton, G. S.: Greenland iceberg melt variability from high-resolution satellite observations, The Cryosphere, 12, 565–575, https://doi.org/10.5194/tc-12-565-2018, 2018.

Gade, H. G.: Melting of ice in sea water: A primitive model with application to the Antarctic ice shelf and icebergs, J. Phys. Oceanogr., 9, 189–198, https://doi.org/10.1175/1520-0485(1979)009<0189:MOIISW>2.0.CO;2, 1979.

Gill, A. E.: Chapter six - adjustment under gravity of a density-stratified fluid, in: Atmosphere–Ocean Dynamics, vol. 30 of *International Geophysics*, pp. 117–188, Academic Press, https://doi.org/10.1016/S0074-6142(08)60031-5, 1982.

Greisman, P.: On upwelling driven by the melt of ice shelves and tidewater glaciers, Deep Sea Res. A, 26, 1051–1065, https://doi.org/10.1016/0198-0149(79)90047-5, 1979.

Hager, A. O., Sutherland, D. A., and Slater, D. A.: Local forcing mechanisms challenge parameterizations of ocean thermal forcing for Greenland tidewater glaciers, EGUsphere, pp. 1–33, https://doi.org/10.5194/egusphere-2023-746, 2023.

Hermann, A. J., Rhines, P. B., and Johnson, E. R.: Nonlinear Rossby adjustment in a channel: beyond Kelvin waves, J. Fluid Mech., 205, 469–502, https://doi.org/10.1017/S0022112089002119, 1989.

Hughes, K. G.: Pathways, form drag, and turbulence in simulations of an ocean flowing through an ice mélange, J. Geophys. Res. Oceans, 127, e2021JC018 228, https://doi.org/10.1029/2021JC018228, 2022.

Hundsdorfer, W., Koren, B., van Loon, M., and Verwer, J.: A positive finite-difference advection scheme, J. Comp. Phys., 117, 35–46, https://doi.org/10.1006/jcph.1995.1042, 1995.

Huppert, H. E. and Turner, J. S.: Ice blocks melting into a salinity gradient, J. Fluid Mech., 100, 367–384, https://doi.org/10.1017/S0022112080001206, 1980.

Hutter, K., Wang, Y., and Chubarenko, I. P.: The role of the Earth's rotation: Oscillations in semi-bounded and bounded basins of constant depth, in: Physics of Lakes: Volume 2: Lakes as Oscillators, pp. 49–113, Springer, https://doi.org/10.1007/978-3-642-19112-1_12, 2011.

Jackson, R. H., Shroyer, E. L., Nash, J. D., Sutherland, D. A., Carroll, D., Fried, M. J., Catania, G. A., Bartholomaus, T. C., and Stearns, L. A.: Near-glacier surveying of a subglacial discharge plume: Implications for plume parameterizations, Geophys. Res. Lett., 44, 6886–6894, https://doi.org/10.1002/2017GL073602, 2017.

Jackson, R. H., Nash, J. D., Kienholz, C., Sutherland, D. A., Amundson, J. M., Motyka, R. J., Winters, D., Skyllingstad, E., and Pettit, E. C.: Meltwater intrusions reveal mechanisms for rapid submarine melt at a tidewater glacier, Geophys. Res. Lett., 47, e2019GL085 335, https://doi.org/10.1029/2019GL085335, 2020.

Jackson, R. H., Motyka, R. J., Amundson, J. M., Abib, N., Sutherland, D. A., Nash, J. D., and Kienholz, C.: The relationship between submarine melt and subglacial discharge from observations at a tidewater glacier, J. Geophys. Res. Oceans, 127, e2021JC018 204, https://doi.org/10.1029/2021JC018204, 2022.

Jenkins, A.: The impact of melting ice on ocean waters, J. Phys. Oceanogr., 29, 2370 – 2381, https://doi.org/10.1175/1520-0485(1999)029<2370:TIOMIO>2.0.CO;2, 1999.

Kajanto, K., Straneo, F., and Nisancioglu, K.: Impact of icebergs on the seasonal submarine melt of Sermeq Kujalleq, The Cryosphere, 17, 371–390, https://doi.org/10.5194/tc-17-371-2023, 2023.

Kang, D. and Fringer, O.: On the calculation of available potential energy in internal wave fields, J. Phys. Oceanogr., 40, 2539–2545, https://doi.org/10.1175/2010JPO4497.1, 2010.

Kelly, S. M., Nash, J. D., and Kunze, E.: Internal-tide energy over topography, J. Geophys. Res. Oceans, 115, https://doi.org/10.1029/2009JC005618, 2010.

Kimura, S., Holland, P. R., Jenkins, A., and Piggott, M.: The effect of meltwater plumes on the melting of a vertical glacier face, J. Phys. Oceanogr., 44, 3099–3117, https://doi.org/10.1175/JPO-D-13-0219.1, 2014.

Klymak, J. M. and Legg, S. M.: A simple mixing scheme for models that resolve breaking internal waves, Ocean Modell., 33, 224–234, https://doi.org/10.1016/j.ocemod.2010.02.005, 2010.

Losch, M.: Modeling ice shelf cavities in a *z* coordinate ocean general circulation model, J. Geophys. Res., 113, C08 043, https://doi.org/10.1029/2007JC004368, 2008.

Magorrian, S. J. and Wells, A. J.: Turbulent plumes from a glacier terminus melting in a stratified ocean, J. Geophys. Res. Oceans, 121, 4670–4696, https://doi.org/10.1002/2015JC011160, 2016.

Malyarenko, A., Wells, A. J., Langhorne, P. J., Robinson, N. J., Williams, M. J., and Nicholls, K. W.: A synthesis of thermodynamic ablation at ice–ocean interfaces from theory, observations and models, Ocean Modell., 154, 101 692, https://doi.org/10.1016/j.ocemod.2020.101692, 2020.

Marshall, J., Adcroft, A., Hill, C., Perelman, L., and Heisey, C.: A finite-volume, incompressible Navier Stokes model for studies of the ocean on parallel computers, J. Geophys. Res., 102, 5753–5766, https://doi.org/10.1029/96JC02775, 1997.

Moon, T., Sutherland, D. A., Carroll, D., Felikson, D., Kehrl, L., and Straneo, F.: Subsurface iceberg melt key to Greenland fjord freshwater budget, Nat. Geosci., 11, 49–54, https://doi.org/10.1038/s41561-017-0018-z, 2018.

Morton, B. R., Taylor, G. I., and Turner, J. S.: Turbulent gravitational convection from maintained and instantaneous sources, Proc. R. Soc. A: Math. Phys. Eng., 234, 1–23, https://doi.org/10.1098/rspa.1956.0011, 1956.

Moyer, A. N., Sutherland, D. A., Nienow, P. W., and Sole, A. J.: Seasonal variations in iceberg freshwater flux in Sermilik Fjord, Southeast Greenland from Sentinel-2 imagery, Geophys. Res. Lett., 46, 8903–8912, https://doi.org/10.1029/2019GL082309, 2019.

Rezvanbehbahani, S., Stearns, L. A., Keramati, R., Shankar, S., and van der Veen, C. J.: Significant contribution of small icebergs to the freshwater budget in Greenland fjords, Commun. Earth Environ., 1, 31, https://doi.org/10.1038/s43247-020-00032-3, 2020.

Schild, K. M., Sutherland, D. A., Elosegui, P., and Duncan, D.: Measurements of iceberg melt rates using high-resolution GPS and iceberg surface scans, Geophys. Res. Lett., 48, e2020GL089 765, https://doi.org/10.1029/2020GL089765, 2021.

Schulz, K., Nguyen, A. T., and Pillar, H. R.: An improved and observationally-constrained melt rate parameterization for vertical ice fronts of marine terminating glaciers, Geophys. Res. Lett., 49, e2022GL100 654, https://doi.org/10.1029/2022GL100654, 2022.

Sciascia, R., Straneo, F., Cenedese, C., and Heimbach, P.: Seasonal variability of submarine melt rate and circulation in an East Greenland fjord, J. Geophys. Res. Oceans, 118, 2492–2506, https://doi.org/10.1002/jgrc.20142, 2013.

Simpson, J. E.: Gravity Currents in the laboratory, atmosphere, and ocean, Ann. Rev. Fluid Mech., 14, 213–234, https://doi.org/10.1146/annurev.fl.14.010182.001241, 1982.

Slater, D. A., Nienow, P. W., Cowton, T. R., Goldberg, D. N., and Sole, A. J.: Effect of near-terminus subglacial hydrology on tidewater glacier submarine melt rates, Geophys. Res. Lett., 42, 2861–2868, https://doi.org/10.1002/2014GL062494, 2015.

Slater, D. A., Goldberg, D. N., Nienow, P. W., and Cowton, T. R.: Scalings for submarine melting at tidewater glaciers from buoyant plume theory, J. Phys. Oceanogr., 46, 1839–1855, https://doi.org/10.1175/JPO-D-15-0132.1, 2016.

Slater, D. A., Carroll, D., Oliver, H., Hopwood, M. J., Straneo, F., Wood, M., Willis, J. K., and Morlighem, M.: Characteristic depths, fluxes, and timescales for Greenland's tidewater glacier fjords from subglacial discharge-driven upwelling during summer, Geophys. Res. Lett., 49, e2021GL097 081, https://doi.org/10.1029/2021GL097081, 2022.

Straneo, F., Curry, R. G., Sutherland, D. A., Hamilton, G. S., Cenedese, C., Våge, K., and Stearns, L. A.: Impact of fjord dynamics and glacial runoff on the circulation near Helheim Glacier, Nat. Geosci., 4, 322–327, https://doi.org/10.1038/ngeo1109, 2011.

Sulak, D. J., Sutherland, D. A., Enderlin, E. M., Stearns, L. A., and Hamilton, G. S.: Iceberg properties and distributions in three Greenlandic fjords using satellite imagery, Ann. Glaciol., 58, 92–106, https://doi.org/10.1017/aog.2017.5, 2017.

Sutherland, D. A., Straneo, F., and Pickart, R. S.: Characteristics and dynamics of two major Greenland glacial fjords, J. Geophys. Res. Oceans, 119, 3767–3791, https://doi.org/10.1002/2013JC009786, 2014.

Wood, M., Rignot, E., Fenty, I., An, L., Bjørk, A., van den Broeke, M., Cai, C., Kane, E., Menemenlis, D., Millan, R., Morlighem, M., Mouginot, J., Noël, B., Scheuchl, B., Velicogna, I., Willis, J. K., and Zhang, H.: Ocean forcing drives glacier retreat in Greenland, Sci. Adv., 7, eaba7282, https://doi.org/10.1126/sciadv.aba7282, 2021.

Xu, Y., Rignot, E., Menemenlis, D., and Koppes, M.: Numerical experiments on subaqueous melting of Greenland tidewater glaciers in response to ocean warming and enhanced subglacial discharge, Ann. Glaciol., 53, 229–234, https://doi.org/10.3189/2012AoG60A139, 2012.

Xu, Y., Rignot, E., Fenty, I., Menemenlis, D., and Flexas, M. M.: Subaqueous melting of Store Glacier, west Greenland from three-dimensional, high-resolution numerical modeling and ocean observations, Geophys. Res. Lett., 40, 4648–4653, https://doi.org/10.1002/grl.50825, 2013.

Yang, R., Howland, C. J., Liu, H.-R., Verzicco, R., and Lohse, D.: Ice melting in salty water: layering and non-monotonic dependence on the mean salinity, J. Fluid Mech., 969, R2, https://doi.org/10.1017/jfm.2023.582, 2023.